J. Dairy Sci. 105:9387–9403
https://doi.org/10.3168/jds.2022-22048

X-ray computerized microtomography and confocal Raman microscopy as complementary techniques to conventional imaging tools for the microstructural characterization of Cheddar cheese

Antonio Lourenco,[1,2] Stephan Handschuh,[2] Mark Fenelon,[1] and Laura G. Gómez-Mascaraque[1]*
[1]Teagasc Food Research Centre, Moorepark, Fermoy, P61 C996 Cork, Ireland
[2]VetCORE–Facility for Research Vienna, University of Veterinary Medicine, 1210 Vienna, Austria

ABSTRACT

This study explored the use of X-ray computerized microtomography (micro-CT) and confocal Raman microscopy to provide complementary information to well-established techniques, such as confocal laser scanning microscopy (CLSM), for the microstructural characterization of cheese. To evaluate the potential of these techniques, 5 commercial Cheddar cheese samples, 3 with different ripening times and 2 with different fat contents, were analyzed. Confocal laser scanning microscopy was particularly useful to describe differences in fat and protein distribution, especially between the 2 samples with different fat contents. The quantitative data obtained through image analysis correlated well with the nutritional information provided in the product labels. Conversely, micro-CT was more advantageous for studying the size and spatial distribution of microcrystals present within the cheese matrix. Two types of microcrystals were identified that differed in size, shape, and X-ray attenuation. The smallest, with a diameter of approximately 10 to 20 μm, were more abundant in the samples and presented a more uniform roundish shape and higher X-ray attenuation. Larger and more heterogeneous crystals with diameters reaching 50 μm were also observed in scarcer numbers and showed lower X-ray attenuation. Confocal Raman microscopy was useful not only for identifying the distribution of all these components but also allowed comparing the presence of micronutrients such as carotenoids in the cheeses and provided compositional information on the crystals detected. Small and large crystals were identified as calcium phosphate and calcium lactate, respectively. Overall, using micro-CT, confocal Raman microscopy, and CLSM in combination generated novel and complementary information for the microstructural and nutritional characterization of Cheddar cheese. These techniques can be used to provide valuable knowledge when studying the effect of milk composition, processing, and maturation on the cheese quality attributes.

Key words: food microstructure, micro-CT, Raman imaging, microcrystal

INTRODUCTION

Cheddar cheese is one of the main cheese varieties produced worldwide (McSweeney et al., 2017). This hard cheese is generally produced by rennet coagulation of pasteurized, standardized cow milk in the presence of starter cultures. The curd is cut, cooked, and separated from the whey, followed by Cheddaring, milling, salting, and pressing (Ong et al., 2017). Cheddar can be ripened for a period that commonly ranges from 3 mo (mild Cheddar) to 1 yr (sharp Cheddar) (Chandan, 2014). The global cheese market represented an approximate value of US $77.6 billion in 2021 and it is expected to grow within the coming years (IMARC, 2022). Cheddar cheese is one of the most-consumed varieties per capita in the United States (Tejeda and Kim, 2021).

Understanding cheese microstructure is essential for new product design and innovation and is considered an important tool for quality control in Cheddar cheese (Ong et al., 2011b). The effects of milk composition and processing variables on cheese functionality as well as sensory and nutritional properties are directly related to a cheese's microstructural properties. The effect of several these variables on the microstructure of Cheddar cheese has been studied, including the renneting pH (Ong et al., 2012), temperature during coagulation (Ong et al., 2011a) and ripening (Soodam et al., 2017), calcium content (Ong et al., 2013; Ong et al., 2015; Ayala-Bribiesca et al., 2016), fat content (Guinee et al., 2000; Rogers et al., 2010), and the age (ripening time) of the cheese (Soodam et al., 2014; Soodam et al., 2015a; Ray et al., 2016).

The most widely used techniques for studying the microstructure of cheese include confocal laser scan-

Received March 4, 2022.
Accepted July 17, 2022.
*Corresponding author: laura.mascaraque@teagasc.ie

ning microscopy (**CLSM**) and electron microscopy techniques. Compared with the more conventional light microscopy, which involves extensive sample preparation and can provide only limited information (Bowland and Foegeding, 2001; Lagaude et al., 2004), the development of CLSM methodologies for the analysis of dairy products (Auty et al., 2001) was an important technological breakthrough, allowing visual differentiation of the lipid and protein fractions of cheese by selective staining with fluorescence dyes. The possibility of optically sectioning cheese samples by confocal imaging techniques can moreover mitigate the disruption caused to fat globules upon physical sectioning in high-fat foods (Ong et al., 2011b). Confocal laser scanning microscopy has therefore been one of the preferred microscopy techniques used to analyze microstructural characteristics of Cheddar cheese in the past 2 decades (Gunasekaran and Ding, 1999; O'Reilly et al., 2003; Soodam et al., 2015a; Anvari and Joyner, 2018). Its main disadvantage, though, is the need for staining the samples if they are not intrinsically fluorescent, which can lead to artifacts.

Because of their capability for higher resolution, electron microscopy techniques, in particular scanning electron microscopy, have also been used as complementary techniques to CLSM (Ong et al., 2011a, 2013; Soodam et al., 2017). However, the sample preparation requirements for imaging under high vacuum involve either dehydrating the samples (Khanal et al., 2018) or intricate, time-consuming, and costly handling and imaging under cryogenic conditions (cryo-scanning electron microscopy) (Lamichhane et al., 2019), thus limiting their widespread application.

X-Ray computerized microtomography (**micro-CT**) is a 3-dimensional (**3D**) imaging technique that exploits variations in X-ray attenuation depending on the composition and density of the different components within a specimen (Willner et al., 2016). This technique is also referred to as X-ray microtomography when it is applied using imaging conditions that allow micrometric resolution. Because the contrast being obtained is based on differences in X-ray absorption, this technique has been more widely used for hard matter, with many applications in material science (Singh et al., 2017), geology (Baker et al., 2012), archeology (Bernardini et al., 2019), and medicine (van den Boogert et al., 2018; Pikhur et al., 2020), among others. In food matrixes, CT and micro-CT have been mainly used to study the internal microstructure of products containing voids, such as foams (Lim and Barigou, 2004; Licciardello et al., 2012), aerated chocolate (Haedelt et al., 2007; Frisullo et al., 2010), or bakery products (Cafarelli et al., 2014; Piovesan et al., 2020). Similarly, CT has been extensively used to study eye formation in Swiss-type cheeses (Huc et al., 2014; Guggisberg et al., 2015; O'Sullivan et al., 2016) and pores caused by freezing in cheese (Conte et al., 2017). The use of CT is facilitated by the high contrast between air and soft materials, but its use in cheese has been mainly limited to the previously mentioned applications (Lei and Sun, 2019). Being a nondestructive technique that allows obtaining quantitative 3-dimensional structural information, its application for studying the microstructure of Cheddar cheese and, in particular, the presence of crystals in this type of product, is evaluated in this work. Cheese crystals have been previously studied and identified through powder X-ray diffraction (Tansman et al., 2014); however, this technique does not provide information on crystal size and spatial distribution.

Confocal Raman microscopy is a hyperspectral imaging technique that provides not only structural but also compositional information of the samples through the analysis of the inelastic scattering of light. Given that Raman spectra are unique for each particular molecule in a specific environment (Butler et al., 2016), every pixel of a Raman micrograph provides invaluable chemical information, which can be obtained with minimal sample preparation and without labeling or staining (Benito-González et al., 2020). Raman microscopy techniques are widely used to explore the microstructure of materials in several disciplines, including forensic sciences (Lv et al., 2016; Zapata and García-Ruiz, 2017), materials engineering (Marcott et al., 2017; Yasseri et al., 2020), or medicine (Zhang et al., 2015; Chaichi et al., 2018). Its application in the characterization of food products has also emerged recently (Roeffaers et al., 2011; Huen et al., 2014; Pu et al., 2019). In dairy, it has been used to understand the microstructure of model food gels containing milk fat (Gómez-Mascaraque et al., 2021) and dairy proteins (Gómez-Mascaraque and Pinho, 2021), as well as complex dairy products such as processed cheese (Smith et al., 2017) or butter (Jensen et al., 2019). Most recently, it was used to differentiate whey protein particles added to a model cheese matrix composed of casein and fat (Nickless and Holroyd, 2020). Regarding commercial cheese samples, D'Incecco et al. (2016) used confocal Raman microscopy to characterize specks and microcrystals in Italian-style extra-hard cheeses, although in this case the authors collected individual spectra of these components rather than mapping the whole cheese matrix. The application of Raman imaging for a comprehensive study of the microstructure of commercial Cheddar cheese products is proposed in this work for the first time.

Table 1. Nutritional information for each Cheddar cheese sample[1]

Component	Sample code				
	LowFat	HighFat	ShortRip	MidRip	LongRip
Fat (g/100 g)	22	35	32	32	32
Carbohydrates (g/100 g)	<0.5	<0.5	0.1	0.1	0.1
Protein (g/100 g)	28	26	26	26	26
Salt (g/100 g)	1.9	1.8	1.7	1.7	1.7
Calcium (g/100 g)	0.75	—	0.69	0.69	0.69
Fat (g/100 g of DM)	42	56	54	54	54
Protein (g/100 g of DM)	54	41	44	44	44

[1]As shown on the product label (top 5 lines) and calculated on a DM basis (2 bottom lines). Dry matter was estimated as the sum of the fat, protein, and salt content in the samples. LowFat = low fat; HighFat = high fat; ShortRip = short ripening; MidRip = mid ripening; and LongRip = long ripening

The objective of this work was to explore the potential of combining different microscopy techniques to maximize the amount of compositional and structural information obtained from commercial Cheddar cheese and similar products. To do so, well-established CLSM and recently developed confocal Raman are combined with micro-CT imaging for determination of cheese structure and nutritional characterization.

MATERIALS AND METHODS

No animals were used in this study, and ethical approval for the use of animals was thus deemed unnecessary.

Cheddar Cheese Samples and Reagents

Two white Cheddar cheese products with different fat contents, referred to as HighFat and LowFat, respectively, were purchased from a local supermarket (Fermoy). Three white Cheddar cheese products with different ripening times, referred to as **ShortRip**, **MidRip**, and **LongRip**, were also purchased from a local supermarket. The relevant nutritional information provided by the suppliers for each cheese type is summarized in Table 1. Calcium lactate pentahydrate, L-tyrosine, L-cysteine hydrochloride hydrate, Nile Red, Fast Green FCF, and 1,2-propanediol were purchased from Sigma-Aldrich.

Confocal Laser Scanning Microscopy

Sample Preparation and Data Acquisition. Internal sections of the commercial cheese samples with an area of approximately 1 cm × 1 cm were cut with a blade and placed on glass microscopy slides before staining. The staining solution consisted of a 50:50 mixture of 0.1% Fast Green FCF (aq.) and 0.02% Nile Red (in 1,2-propanediol), which is a combination of dyes commonly used to observe the distribution of fat (stained by Nile Red) and protein (stained by Fast Green FCF) in cheese samples (Soodam et al., 2015b). The staining solution (approximately 100 μL) was gently deposited on the surface of the samples and the dyes were allowed to diffuse in during 30 min under refrigeration at 4°C to prevent the mobility of liquid fat, as suggested by Ong et al. (2011b). The excess staining solution was then gently removed with a tissue and the samples were covered with 0.13-mm coverslips.

Stained samples were observed using a Leica TCS SP5 confocal laser scanning microscope (Leica Microsystems CMS GmbH) using a 63 × /1.4 oil immersion objective and maintaining the pinhole diameter at 1 Airy Unit. A digital zoom of 2 was applied. Fast Green FCF was excited at 633 nm using a He/Ne laser, and the corresponding emission filter was set at 650 to 705 nm. Nile Red was excited at 488 nm using a diode-pumped solid-state laser, and the corresponding emission filter was set at 563 to 610 nm. Leica LAS AV software (v 2.7.3.9723; Leica Microsystems CMS GmbH) was used to acquire digital images 1,024 × 1,024 pixels in size. Each line was averaged 3 times to increase signal-to-noise ratio. Each sample was prepared for imaging in duplicate, and at least 3 different areas of each replica were imaged to ensure that the obtained images were representative of the samples.

Data Processing and Image Analysis. Confocal images (*.LIF files) were imported into FIJI (Schindelin et al., 2012) and exported as RGB color overlays in *.TIFF format. Based on these color overlay images, protein and fat areas were segmented by pixel classification using the machine learning software Ilastik (Sommer et al., 2011; Berg et al., 2019). The pixel classification was achieved after training the classifier to separate the object classes (i.e., fat, protein and unstained) by drawing annotations and evaluating the interactive prediction in a live update mode, followed by drawing additional annotations. This operation was

performed on a subset of 3 images. Segmentation masks were saved in *.TIFF format and again imported into FIJI for area measurements.

Statistical Analysis

The statistical analysis was performed on software OriginPro 2019 version 9.6.0.172. Analysis of variance assumptions were tested by using the Kolmogorov–Smirnov test to check for normality and the Brown–Forsythe test to check for homogeneity of variance. Analysis of variance post-hoc analyses were carried out with the Tukey test. The level of significance chosen was $\alpha = 0.05$.

X-Ray Microtomography

Sample Preparation and Data Acquisition. Cheddar cheese samples were cut with a scalpel from an internal area of the cheese sample into a cube with sides that were approximately 2.5 mm. The samples were then carefully placed inside 10-μL pipette filter tips, sitting on top of its filter. To prevent loss of moisture and consequent deformation of the sample during the image acquisition, water was added to the bottom of the tip (without touching the filter) and the bottom sealed with Parafilm. To prevent the sample from moving inside the tip, a paper towel was placed above the cheese. Pre-moisturized paper was also added to the top of the tip and Parafilm was used to seal it (Supplemental Figure S1, https://doi.org/10.17632/4h2gwr26p9.1; Lourenco et al., 2022). One sample of each cheese type was analyzed.

The mounted Cheddar samples were scanned with an XRadia MicroXCT-400 (Carl Zeiss X-ray Microscopy) using the 40× detector assembly. X-Ray source settings were 40 kVp/200 μA, and no X-ray filter was used. Projection images were recorded over a 360° rotation with 5 s exposure per projection (detector binning = 2) and an angular increment of 0.225° between projections. Tomographic sections were reconstructed with the software XMReconstructor (Carl Zeiss X-ray Microscopy) supplied with the scanner and saved as DICOM sequences. Isotropic voxel resolution in the reconstructed volumes was 0.51 μm.

For one sample (MidRip) 2 scans with larger fields of view and lower resolutions were additionally acquired. These scans were made from larger pieces of cheese and again acquired with an XRadia MicroXCT-400 using the 0.4× (sample diameter = 10 mm, isotropic voxel size of 9.46 μm) and the 10× (sample diameter = 3 mm, isotropic voxel size of 2.26 μm) detector assembly. The lower resolution scans aimed to provide structural information on a bigger scale, in particular on the spatial distribution of microcrystals, given the scarcity of one of the types of crystals identified in the high-resolution images.

Data Processing and Image Analysis. Dicom sequences were imported into the 3D software package Amira 2019.4 (FEI SAS; part of Thermo Fisher Scientific). Subsequently, image volumes were filtered using a 3D Bilateral filter (kernel size = 3 × 3 × 3) for noise reduction. The *AutoThresholding* tool (Type: Auto Threshold High; Interpretation: 3D; Model: min-max; Criterion: entropy) was used to determine a threshold that separates the crystals from the rest of the cheese matrix for each scan. These thresholds were used for segmentation of microcrystals in the *SegmentationEditor*. For samples containing 2 types of crystals, the larger crystals were manually selected using the *Pick&Move* tool and assigned to a separate material. Based on the segmentation masks, the single crystals were separated on the basis of connectivity using the tool *Labeling*. Finally, the number of crystals and the mean particle volume were calculated with the *LabelAnalysis* tool (a correction was applied for particles that touched the border of the analysis region of interest: for particle counting, each border particle was counted as 0.5 particles; for analysis of mean particle volume, border particles were excluded). Particles below 100 μm^3 were excluded from the analysis. The 3D surface renderings were created using the Amira *SurfaceGen* tool.

Furthermore, the volume rendering software Drishti (Limaye, 2012) was used to visualize the size, shape, and 3D distribution of microcrystals. Due to the high density of microcrystals, we only rendered a subvolume of 500 × 500 × 500 voxels (257.2 × 257.2 × 257.2 μm) from each data set.

Descriptive statistics and box plotting were performed using OriginPro 2019 version 9.6.0.172. Interquartile range (**IQR**) was used to identify outliers: 3 × IQR > outliers > 1.5 × IQR.

Confocal Raman Microscopy

Data Acquisition. An Alpha300 R confocal Raman microscope (WITec) with a 532-nm laser was used for all the confocal Raman microscopy analyses. Internal sections of the cheese samples (2–3 mm thick) cut with a blade were placed on glass microscopy slides. A method previously reported was used for confocal Raman imaging (Gómez-Mascaraque et al., 2021). Specimens with an area of 500 × 500 μm were scanned at 250 points per line × 250 lines per image, and spectra were collected using a 50×/0.55 air objective, a laser power of 60 mW, and an integration time of 0.33 s (1 accumulation). Spectra were collected from the internal

Table 2. Assignment of the main Raman bands from the cheese samples

Wavenumber (cm^{-1})	Identification[1]	Main cheese component	References
1,748	ν(C = O)	Fat	Gallier et al., 2011; Czamara et al., 2015; Smith et al., 2017; Gómez-Mascaraque et al., 2021
1,662	ν(C = C)	Fat	Gallier et al., 2011; Czamara et al., 2015; Smith et al., 2017; Gómez-Mascaraque et al., 2021
1,619	Tyrosine	Protein	Smith et al., 2017
1,527	Carotenoids	Carotenoids	Smith et al., 2017; Gómez-Mascaraque et al., 2021
1,448	α(–CH_2)	Fat	Czamara et al., 2015; Gómez-Mascaraque et al., 2021
1,305	τ(–CH_2)	Fat	Czamara et al., 2015; Gómez-Mascaraque et al., 2021
1,274	δ(= CH) and amide III	Fat/protein	Czamara et al., 2015; Smith et al., 2017; Gómez-Mascaraque et al., 2021
1,164	ν(C–C), carotenoids	Carotenoids	Smith et al., 2017; Gómez-Mascaraque et al., 2021
1,135	ν(C–C)	Fat	Czamara et al., 2015; Gómez-Mascaraque et al., 2021
1,070	ν(C–C)	Fat	Gallier et al., 2011; Czamara et al., 2015; Smith et al., 2017; Gómez-Mascaraque et al., 2021
1,011	Phenylalanine[2]	Protein	Smith et al., 2017
877	C–O–O	Fat	Czamara et al., 2015; Gómez-Mascaraque et al., 2021

[1]ν: stretching; δ: deformation; α: scissoring; τ: twisting.

[2]This band was slightly shifted to higher wavenumbers with respect to that reported in previous works due to an overlap with one of the bands ascribed to calcium phosphate (refer to detailed discussion in the section "Analysis by Confocal Raman Microscopy").

structure of the cheese (about 25 μm below the surface). The software WITec Control Five v5.0 (WITec) was used for data acquisition.

Data Processing and Image Analysis. The raw spectra were corrected by using a cosmic ray removal correction function (filter size 3, dynamic factor 8) and a shape function for background subtraction (shape size 250, noise factor 1) using the WITec Project Five software (v5.0). Both univariate and multivariate analyses of the spectral data were performed to map the distribution of different components in the cheese samples, based on previously published methods (Benito-González et al., 2020; Gómez-Mascaraque and Pinho, 2021).

The univariate analysis method was based on the integration of narrow spectral ranges considered of particular interest, summarized in Table 2. The intensity of each pixel in the images obtained through this method represents the area under the spectrum in the selected spectral ranges for that specific measurement point.

The multivariate analysis method considered the full Raman spectra to map the different components in the cheese samples by applying the basis analysis algorithm, which describes each measured spectrum of a hyperspectral data set $\left(\overrightarrow{S_i}\right)$ by a linear combination of a basis spectra, as described in Equation 1, where $\overrightarrow{H_i}$ is the mixing value for spectrum i, $\overrightarrow{E_i}$ is the error spectrum, and $\hat{B}$ is the matrix of basis spectra. The mixing values $\left(\overrightarrow{H_i}\right)$ are obtained by the method of least squares:

$$\overrightarrow{S_i} = \hat{B}\overrightarrow{H_i} + \overrightarrow{E_i}. \quad [1]$$

The method followed to generate the matrix of basis spectra was iterative. The most intense spectrum from the whole data set was selected as the first basis spectrum, and the residual image was then generated. Subsequent cycles of selecting an additional basis spectrum and calculating the corresponding residual images were performed until the user considered that the obtained residual image depicted just noise (Benito-González et al., 2020). The basis spectra were then averaged and de-mixed.

RESULTS AND DISCUSSION

Microstructural Analysis by CLSM

Figure 1 shows representative CLSM micrographs for each of the 5 commercial Cheddar cheese samples analyzed (replicates can be seen in Supplemental Figure S2, https://doi.org/10.17632/4h2gwr26p9.1; Lourenco et al., 2022). Fat and protein were selectively stained and their distribution mapped within the cheese matrix. The observed structure resembled that for noncommercial Cheddar cheese samples analyzed in previous works (Ong et al., 2013; Soodam et al., 2014). All samples exhibited a dense matrix typical of close-textured hard cheeses (Chandan, 2014).

As expected, the fat distribution in the 2 cheese samples with varying fat contents was markedly different. The LowFat sample exhibited smaller and more spherical fat globules (Figure 1a), and the fat globules in the HighFat cheese were fused into bigger clumps with nonspherical shapes (Figure 1b). This observation is consistent with previous studies in which a series of Cheddar cheeses with increasing fat contents showed

Table 3. Distribution of components found in the confocal laser scanning micrographs (average ± SD)

	Sample code				
Component	LowFat[1]	HighFat[1]	ShortRip[2]	MidRip[2]	LongRip[2]
Fat	36.14 ± 0.04%	50.04 ± 0.01%	39.52 ± 0.01%	41.08 ± 0.02%	34.64 ± 0.04%
Protein	61.45 ± 0.04%	49.32 ± 0.01%	53.83 ± 0.03%	49.24 ± 0.02%	58.04 ± 0.02%
Unstained	2.41 ± 0.002%	0.64 ± 0.003%	6.65 ± 0.03%	9.69 ± 0.03%	7.32 ± 0.02%

[1]Low fat (LowFat) versus high fat (HighFat) ANOVA: fat, $P = 0.0019$; protein, $P = 0.0057$; unstained, $P = 0.9811$.

[2]Two-way ANOVA pairwise comparisons for the components protein, fat, and unstained area between the short ripening (ShortRip), mid ripening (MidRip), and long ripening (LongRip) samples: $P > 0.05$.

greater extents of fat globule aggregation and coalescence (Guinee et al., 2000; Rogers et al., 2010). The fraction of fat estimated through quantitative image analysis was significantly lower ($P = 0.0019$) for LowFat than for HighFat samples (Table 3). Consequently, the mean protein content of these 2 cheeses was significantly different ($P = 0.0057$). No statistically significant difference was found between the unstained areas of these 2 cheeses ($P = 0.9811$) (Table 3).

Samples with different maturation times had similar fat distributions to that of the HighFat cheese (Table 1), featuring a considerable amount of coalesced nonglobular fat. No clear correlations could be identified between the ripening time and microstructure of the cheeses. When a 2-way ANOVA was carried out, all the pairwise comparisons were not statistically significant ($P > 0.05$) for the components protein, fat, and unstained areas among the cheeses with the 3 ripening times. Rogers et al. (2010) observed no major structural changes during ripening of Cheddar cheeses, and Soodam et al. (2015a) reported only minimal structural changes. Indeed, as suggested by Guinee et al. (2000), because fat is mostly solid at the usual ripening temperatures no further aggregation or significant migration of the globules would be expected during maturation. Therefore, the structural differences between these 3 commercial samples could not be directly attributed to their ripening time.

It is worth noting that the unstained areas observed in the CLSM micrographs of the Cheddar cheese samples, which do not correspond to either fat or protein, have been generally attributed to pores in the cheese matrix (Ong et al., 2011a; Soodam et al., 2017). However, some of these unstained areas had a very

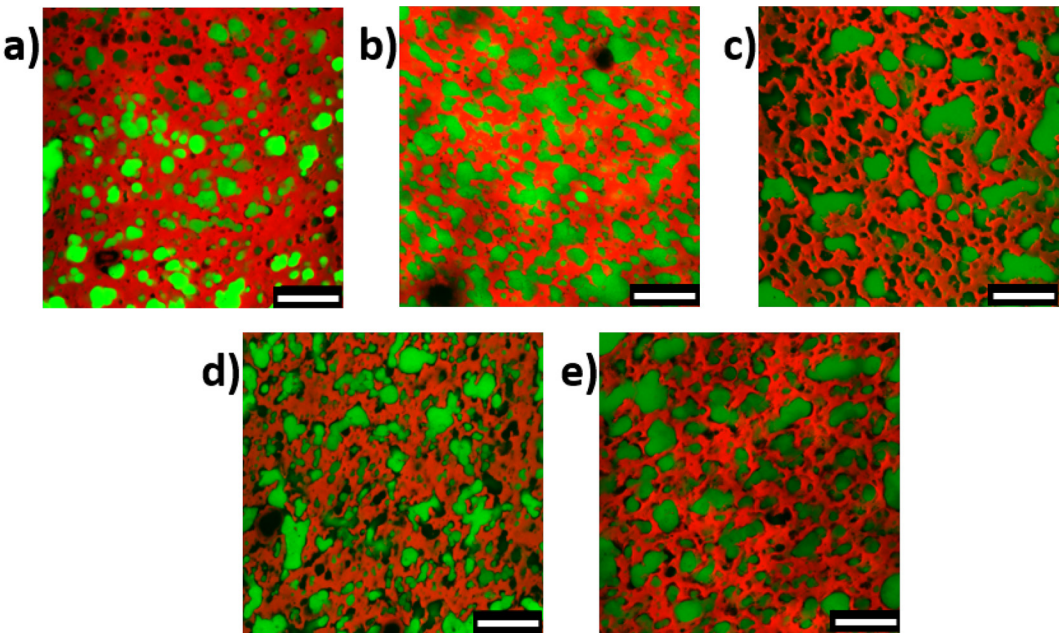

Figure 1. Confocal laser scanning micrographs of the 5 commercial Cheddar cheese samples: (a) low fat, (b) high fat, (c) short ripening, (d) mid ripening, and (e) long ripening. The Nile Red-stained fat is shown in green, and the Fast Green FCF-stained protein is shown in red. The length of the scale bars corresponds to 25 μm.

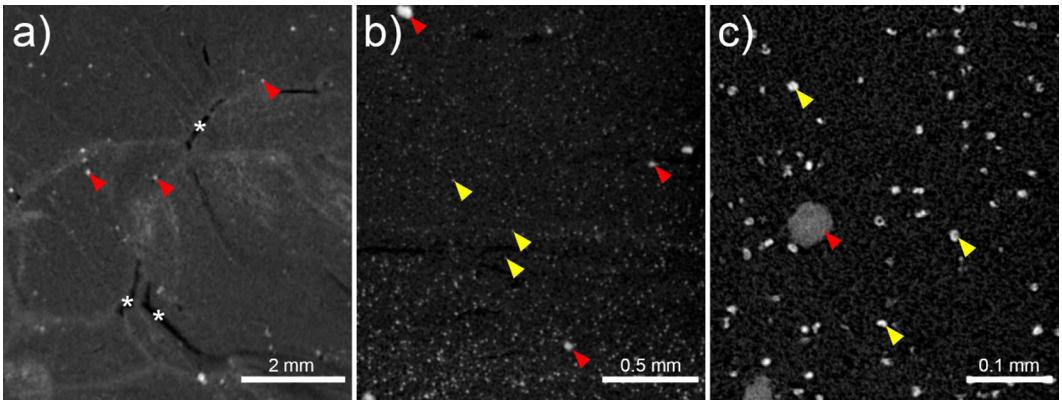

Figure 2. X-Ray computerized microtomography slices from the mid-ripening sample acquired using different detector assemblies: (a) 0.4× overview scan (9.46 μm voxel size) showing the overall structure of the cheese including air-filled voids (asterisks) and large microcrystals (red arrowheads), (b) 10× scan (2.26 μm voxel size) spatially resolving small microcrystals (yellow arrowheads) and showing their heterogeneous spatial distribution, (c) 40× scan (0.51 μm voxel size) showing clear differences in X-ray attenuation between small and large microcrystals, as well as differences in X-ray attenuation between protein and fat.

well-defined circular shape, which suggested that they might correspond to the microcrystals identified using micro-CT and confocal Raman microscopy (see sections "Microstructural Analysis by Micro-CT" and "Analysis by Confocal Raman Microscopy"), with a similar range of sizes (approximately 7–13 μm).

Microstructural Analysis by Micro-CT

It was possible to observe microcrystals embedded in the cheese matrix because they had considerably greater X-ray attenuation compared with other components. This is particularly relevant because crystals affect visual and textural properties and are not easily studied using the conventional CLSM technique due to the difficulty of staining them.

Two different types of microcrystals were identified in the samples based on apparent differences in size and X-ray attenuation. Large microcrystals can already be observed in low resolution micro-CT scans (Figure 2a); however, small microcrystals are spatially resolved only in higher-resolution scans (Figure 2b,c). The smaller ones, with a diameter of approximately 10 to 20 μm, showed greater X-ray attenuation and were present in greater amounts in the samples, whereas the bigger crystals were much scarcer and very heterogeneous in size and shape, with diameters of about 50 μm (Figure 3A–E). The spatial distribution of both small and large microcrystals was quite heterogeneous (Figure 2a,b).

Figure 3F and G shows the size distribution of each of the crystal types in each cheese sample. Regarding the smaller crystals (Figure 3F), a small interquartile range and the mean close to the median, with an approximate value of 5×10^2 to 10^3 μm^3, was observed, indicating some degree of crystal size uniformity in each sample. However, the LongRip cheese showed a higher median and mean than the other cheese samples of approximately 4×10^3 μm^3. It was also possible to observe a large number of higher volume outliers for all samples, indicating the presence of crystal clusters. This shows that the segmentation process was unable to individualize crystals, mostly due to the shape roughness of these crystals. The number of crystals detected and their overall percentage representation in the analyzed cheese matrix is shown in Table 4. Generally, a high number of small crystals (>2,000) were detected in the majority of the samples. However, in HighFat and LongRip samples, overall approximately 4 times fewer crystals were detected (Table 4), which can also be visually observed in Figure 3B and E.

The larger crystals were not detected in the analyzed volumes of the LowFat and LongRip cheese samples. However, this was not because large microcrystals are generally absent in these types of cheese, but rather because of their scarcity in the cheese matrix. Large microcrystals could be detected in the X-ray preview projection images depicting the whole 2.5 × 2.5 × 2.5 mm cheese cube for both samples. For the other 3 cheese samples, large microcrystals were detected in the analyzed volumes and they were in average from 10^4 to 10^5 μm^3.

D'Incecco et al. (2016) evaluated the number of crystals in 18- to 20-mo ripened Italian-style extra-hard cheeses and observed numbers that ranged from 30 to 100 crystals/mm^2. The authors also observed that a lower amount of crystals was detected in younger cheeses. That was not the case in this work—the number of small crystals detected by micro-CT was larger for both ShortRip and MidRip samples than for the LongRip sample. However, an increase in the average size of the

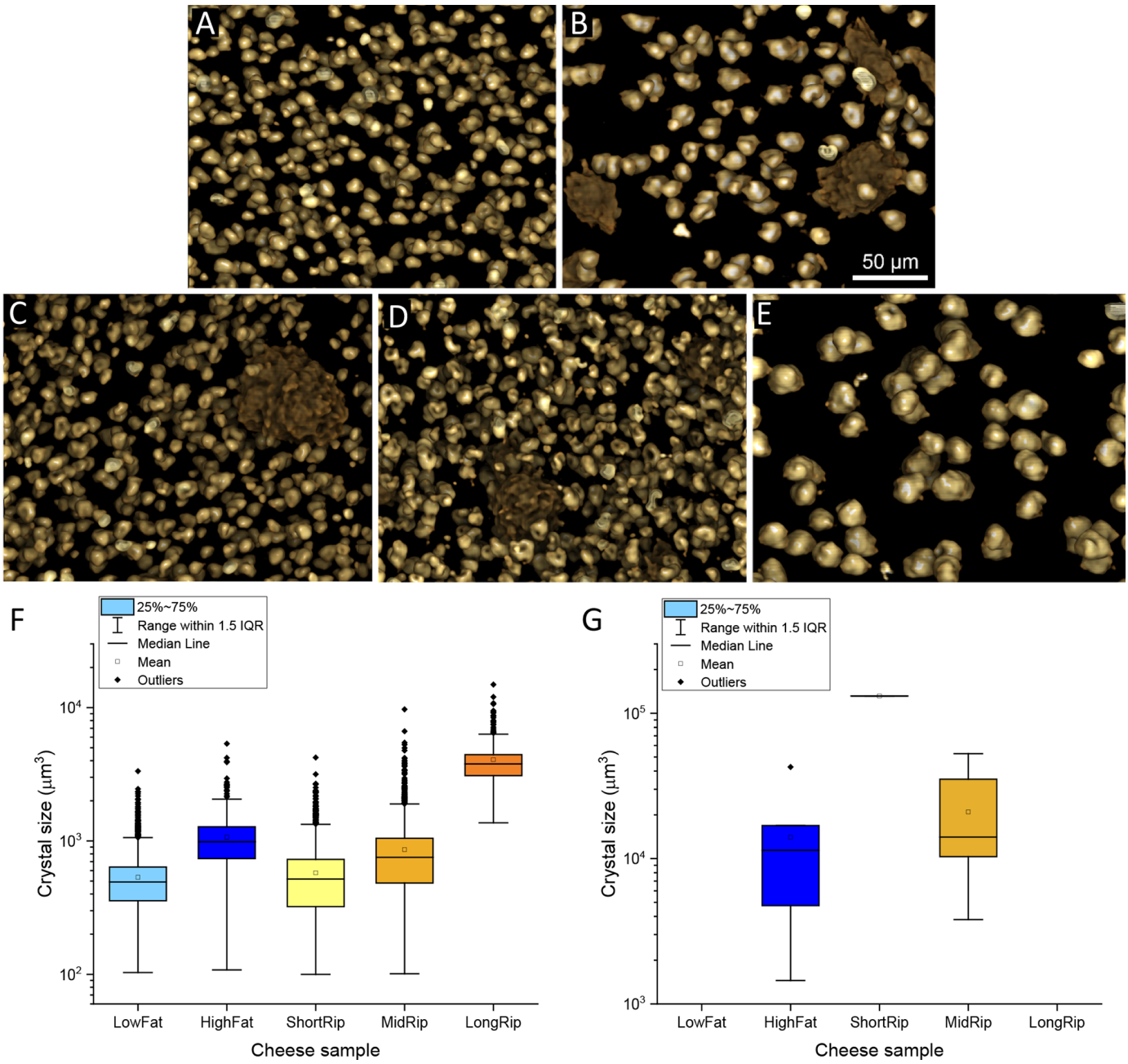

Figure 3. Microcrystals detected in cheese samples: volume renderings of small (bright gold) and large (dark gold) crystals obtained from (A) low fat (LowFat); (B) high fat (HighFat); (C) short ripening (ShortRip); (D) mid ripening (MidRip); and (E) long ripening (LongRip) cheese samples and box-plot representations of volumetric size distribution (>100 µm^3) observed for the small (F) and large (G) crystals in each of the cheese samples. IQR = interquartile range.

crystals during ripening was observed (both mean and median).

These data demonstrate that the applied methodology can quantify the number and size of microcrystals in Cheddar cheese samples. However, data regarding the number of microcrystals per volume should be interpreted with caution because in the present study only a small subvolume (roughly 0.06 mm^3) was scanned and analyzed for each Cheddar sample. Considering the heterogeneous spatial distribution of small and large microcrystals in the Cheddar matrix (Figure 2b), the presented data may be biased by sampling site. As discussed above, the small areas analyzed may be responsible for the absence of large microcrystals in

Table 4. Characterization of crystals detected with X-ray computerized microtomography[1]

Cheese sample	Crystal		Standardized number of crystals per mm^3			Total volume of cheese matrix analyzed (mm^3)
	Type	Volume (%)	Uncorrected	Corrected	>100 μm^3	
LowFat	Small	1.76	37,424	30,068	28,966	0.059
	Large	—	—	—	—	
HighFat	Small	0.87	9,547	7,594	7,281	0.064
	Large	0.16	141	109	109	
ShortRip	Small	1.90	38,948	32,138	29,224	0.058
	Large	0.49	69	17	17	
MidRip	Small	2.55	38,631	30,538	25,723	0.065
	Large	0.39	169	154	154	
LongRip	Small	1.99	9,349	6,032	3,968	0.063
	Large	—	—	—	—	

[1]LowFat = low fat; HighFat = high fat; ShortRip = short ripening; MidRip = mid ripening; and LongRip = long ripening. — = no crystals detected in the total volume analyzed.

the 2 scans and affect the absolute numbers of small microcrystals per volume (Table 4). Future studies investigating a larger number of subvolumes for each type of Cheddar are needed to provide statistically meaningful data on the number of small and large microcrystals that are representative of the different types of Cheddar; this was beyond the scope of the present work. Furthermore, it needs to be mentioned that the segmentation procedure is critically important for all subsequent steps of image analysis, including particle counting and particle volume measurements. Thus, for all samples the segmentation masks that were generated by automated thresholding were validated by visual inspection.

Several crystals have previously been identified in Cheddar cheese, including calcium lactate pentahydrate, tyrosine, cysteine, and calcium phosphate crystals (Tansman et al., 2015). Although the micro-CT analysis allowed quantification and provided valuable information on the size/shape and distribution (Figure 3) of the 2 types of crystals found in the cheese samples, complementary techniques (usually based on chemical analysis or X-ray diffractometry) are needed to be able to identify them. Raman microscopy was used to identify these 2 types of crystals (see "Analysis by Confocal Raman Microscopy").

High-resolution micro-CT images also allowed visual differentiation between protein and fat in the cheese matrix due to differences in X-ray attenuation (Figure 2c). However, scans did not segment and measure protein and fat content as accurately as in CLSM images. This is because, compared with the CLSM (Figure 1), micro-CT scans showed both a lower protein/fat contrast (monochromatic vs. selective fluorescent 2-color labeling) and also a lower spatial resolution. Synchrotron micro-CT could be used to acquire higher-resolution scans that would potentially make accurate protein/fat content measurements feasible.

Analysis by Confocal Raman Microscopy

Averaged Raman Spectra and Compositional Information. One of the advantages of Raman microscopy is the possibility of obtaining not only structural information but also compositional information about specimens. To elucidate potential compositional differences among the cheese samples, the whole spectra data set acquired for each of them, consisting of 62,500 spectra for each scanned area, was averaged and compared. Figure 4 shows the normalized average Raman spectra for the 5 cheese samples.

The most intense bands observed in all cases were those attributed to the stretching and bending vibrations of aliphatic residues (CH_3, CH_2, and CH groups) present in all proteins, fats, and carbohydrates in the range of about 2,800 to 3,000 cm^{-1} (Czamara et al., 2015; Stephani et al., 2017). However, it is the region of the spectra between 500 and 2,000 cm^{-1} (the fingerprint region) that is the most commonly used to identify different components because of its greater specificity. The most relevant bands found in this region are identified in Table 2 based on previous works (Gallier et al., 2011; Czamara et al., 2015; Smith et al., 2017; Gómez-Mascaraque et al., 2020).

The spectra of the group of Cheddar cheese samples featuring different ripening times were very similar, as expected, given their same macronutrient composition (Table 1). In contrast, the 2 Cheddar cheese samples with different fat contents exhibited notably different spectra. Differences were observed in the band attributed to water, which was expected to be more intense for the LowFat cheese, given the lower percentage of solids in this sample (Table 1). Reducing fat levels leads to increased protein and moisture in the nonfat substance. Processing parameters are often adjusted during manufacture to improve cheese texture and quality attributes (Fenelon and Guinee, 1999; Guinee et al., 2007). Clear

differences were also observed in the fingerprint region of the spectra. In particular, the bands attributed to carotenoids centered at 1,527 and 1,164 cm^{-1} were considerably more intense in the full-fat cheese sample. Although carotenoids are micronutrients present in very low concentrations in dairy products, the charac-

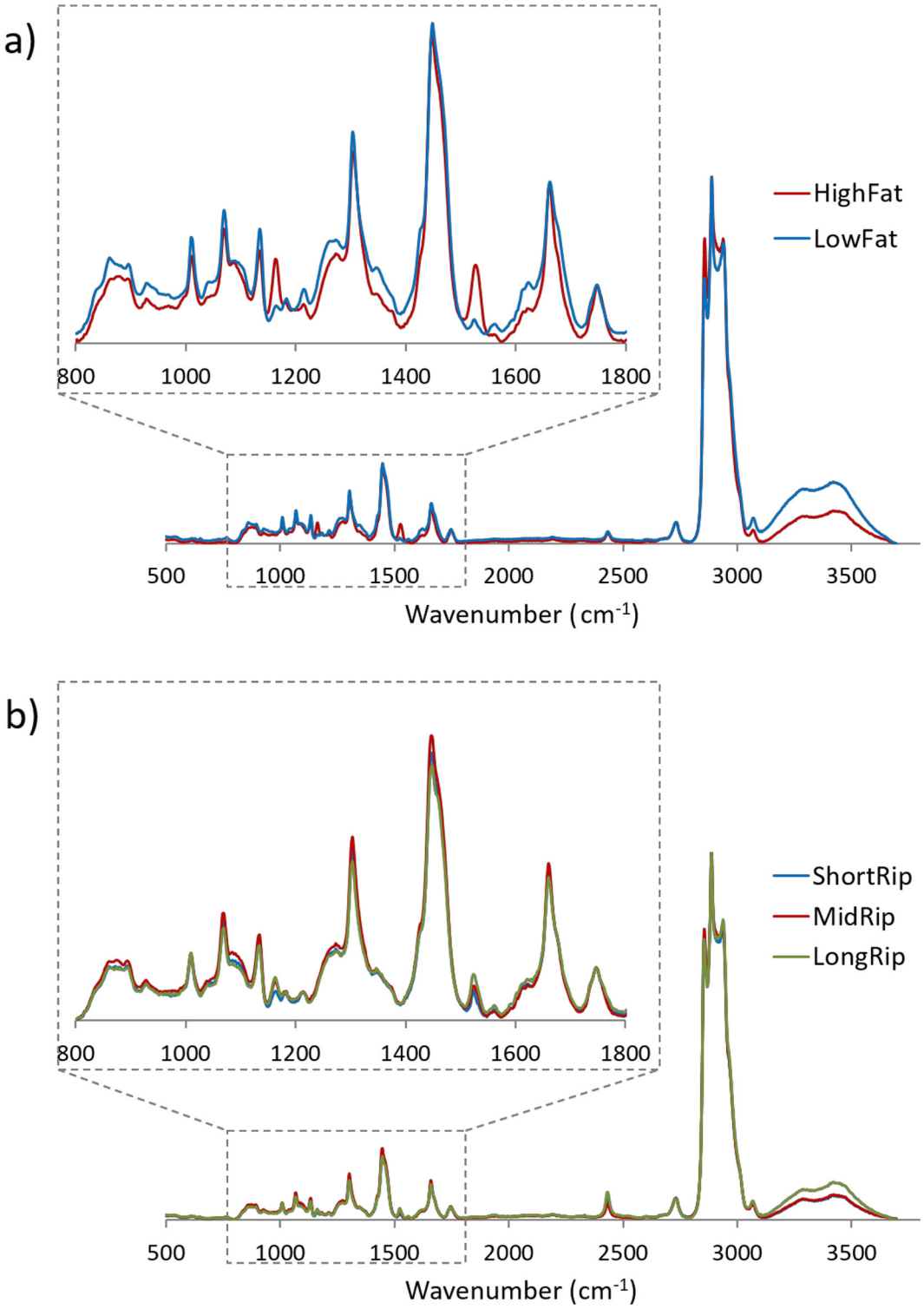

Figure 4. Average and normalized Raman spectra of cheese samples with different fat content (a) and different ripening times (b). LowFat = low fat; HighFat = high fat; ShortRip = short ripening; MidRip = mid ripening; and LongRip = long ripening.

teristic conjugated double bonds in their structure yield strong Raman bands. Consequently, small variations in the content of this micronutrient in dairy products are more easily detected by Raman spectroscopy than for other components. Being lipophilic compounds, carotenoids are found in the lipid fraction of milk and dairy products. Thus, the higher content of these compounds detected in the full-fat cheese sample correlates well with the greater concentration of fat in that sample. Other relevant bands that showed differences in intensity for these 2 cheese samples include those attributed to proteins in cheese, centered at 1,619 and 1,274 cm^{-1} (Table 2). These were slightly more intense for the low-fat cheese sample, which was consistent with its higher protein/fat ratio compared with the full-fat cheese.

Structural Information Through Univariate Data Analysis. Different data processing approaches have been proposed to study the distribution of different components in the samples at the microstructural level using Raman microscopy, which can be divided into 2 main groups: univariate and multivariate analyses (Gómez-Mascaraque and Pinho, 2021). Smith et al. (2017) showed that a simple univariate analysis based on integrating specific spectral regions allowed mapping of the distribution of protein, fat, water, and trisodium citrate in processed cheese. A similar approach was used in this work to map the distribution of fat, protein, water, and carotenoids in the commercial Cheddar cheese samples, using the characteristic bands summarized in Table 2. As a representative example, Figure 5 shows the individual Raman images obtained for the HighFat sample using the different spectral regions.

Most of the bands attributed to fat, especially the ones centered at 1,305 and 1,448 cm^{-1}, and the region corresponding to water (3,100–3,600 cm^{-1}) provided a good contrast between pixels rich in these components and pixels with a low fat and water content (Figure 5). However, from the 3 characteristic bands selected for protein, only the peak generally attributed to phenylalanine residues, centered at 1,011 cm^{-1} in the obtained spectra, yielded structured images. The other two resulted only in noise. Indeed, the Raman signal of proteins is considerably weaker than that of fats, and in many cases, overlaps exist between both components. This is one of the limitations of Raman microscopy, despite its many advantages. Smith et al. (2017) also reported that imaging of the protein distribution in processed cheese was mainly achieved by using the phenylalanine band. Interestingly, the integration of this spectral region for the commercial Cheddar samples revealed very defined, micro-spherical features that resembled the smallest crystals detected in the micro-CT scans of the samples and not the distribution of protein (Figure 5). The nature of these crystals was further investigated using the multivariate analysis approach (see "Structural Information Through Multivariate Data Analysis"). Regarding the bands attributed to carotenoids, their intensity decreased from top to bottom, following the direction of scanning, suggesting a photo-degradation effect. This has been previously observed for other samples containing carotenoids (Gómez-Mascaraque et al., 2021) and precluded obtaining structural information from these bands.

Structural Information Through Multivariate Data Analysis. A multivariate analysis approach was also applied to maximize the amount of information obtained from the spectral data sets, following the method detailed in the section "Data Processing and Image Analysis." Up to 4 different components were identified in the Cheddar cheese samples, 3 of which were common to all of the sample data sets. Figure 6 shows the spectra obtained for the MidRip sample, which presented the 4 components. Supplemental Figure S3 (https://doi.org/10.17632/4h2gwr26p9.1; Lourenco et al., 2022) shows the spectra obtained for the rest of the samples. The spectrum of component b (Figure 6b) exhibits all the characteristic bands of fat and resembles those reported for anhydrous milk fat (Gómez-Mascaraque et al., 2021) and butter (Gómez-Mascaraque et al., 2020). On the other hand, the spectrum of component c (Figure 6c) shows the characteristic peaks of proteins and water, similar to those reported for protein hydrogels (Gómez-Mascaraque and Pinho, 2021). Therefore, in contrast to the univariate analysis method, the multivariate processing approach successfully identified the 3 main components of Cheddar cheese: protein, fat, and water. The fact that protein and water were identified as a single component was not surprising, given that water is indeed embedded in the casein hydrogel network of cheese. As discussed below, 2 additional components were identified that were attributed to the presence of crystals in the cheese samples.

Figure 7 shows the distribution of the identified components in the 5 commercial Cheddar cheese samples. Supplemental Figure S4 (https://doi.org/10.17632/4h2gwr26p9.1; Lourenco et al., 2022) compares, for 2 of the samples, these images obtained through multivariate processing to the equivalent images obtained using the univariate analysis method, created by combining the data of the individual spectral regions (the band of water was used to map the distribution of protein, because none of the bands attributed to protein, explored in the section "Structural Information Through Univariate Data Analysis," were successful). The images obtained through the univariate analysis were noisier due to the overlap of the signal from the different components. In contrast, the multivariate analysis led to more clearly defined distributions of components.

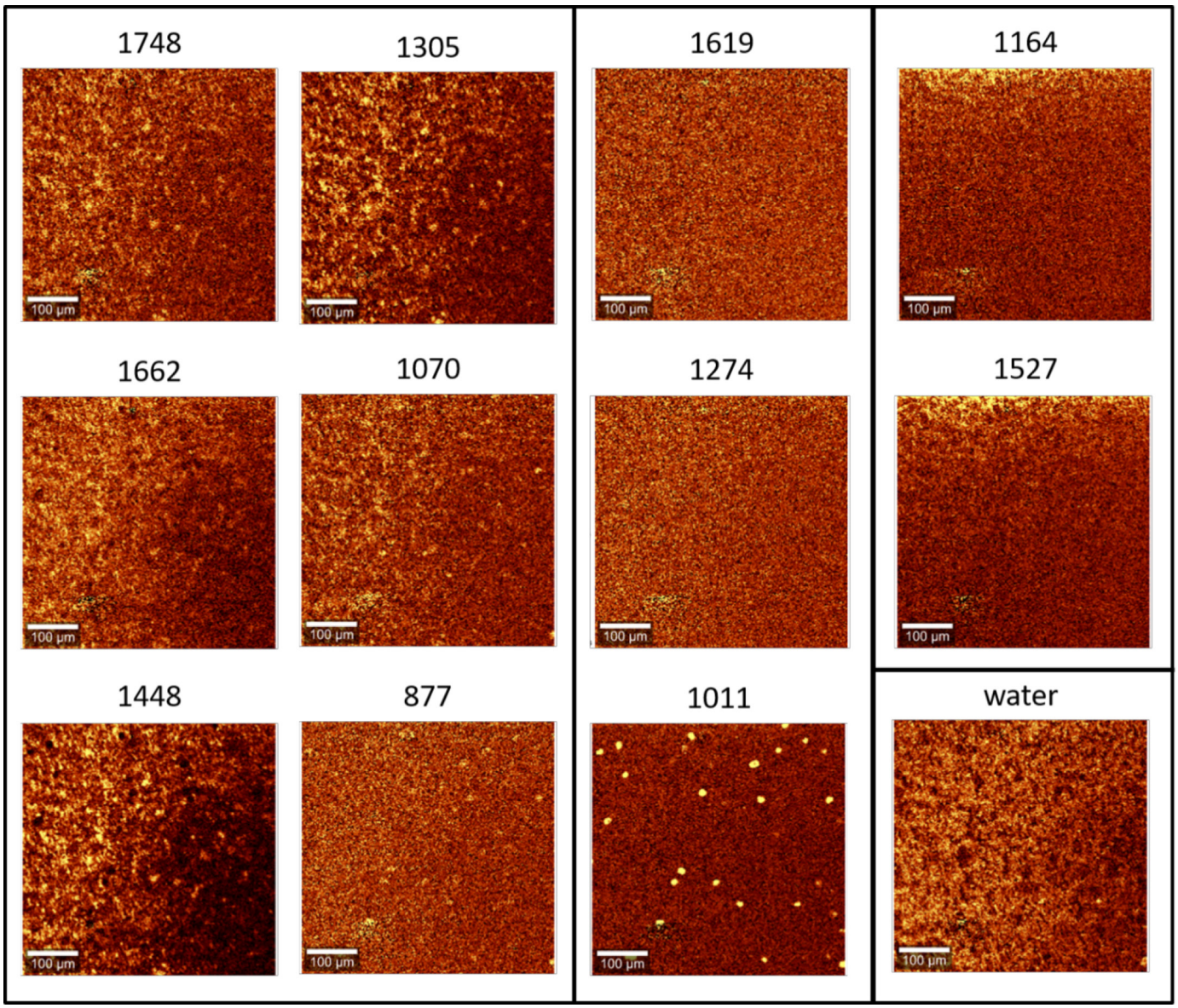

Figure 5. Raman images of the commercial Cheddar cheese sample designated as high fat obtained using the univariate data analysis approach. The numbers on the images indicate the wavenumber (cm^{-1}) at the center of the spectral regions used to build each image. Lighter pixels denote a greater signal intensity, and darker pixels correspond to lower intensities at the specified wavelengths.

The smaller fat globule size and larger protein area previously observed through CLSM for the LowFat sample compared with the HighFat sample were also evidenced in the Raman micrographs, scanned across a larger area compared with the former technique, which allowed observing additional features such as the presence of curd junctions. These curd junctions, which are formed by fusion of curd particles during pressing in Cheddar cheese manufacturing, contain more protein and less fat than other regions of the cheese matrix (Kalab et al., 1982), and this could be visually observed in the Raman micrographs of some samples (white arrows in Figure 7c, d, e). On the other hand, the chemical information intrinsic to the spectral data sets facilitated the identification of additional components (other than fat and protein) that are not easy to stain (e.g., crystals).

Two different classes of microcrystals were identified in the cheese samples by Raman microscopy, as also detected in the micro-CT scans. The smallest and more abundant ones exhibited an intense peak centered around 995 cm^{-1}, and a less intense band centered at 886 cm^{-1}, which were consistent with calcium phosphate microcrystals identified in Italian-style hard cheeses by

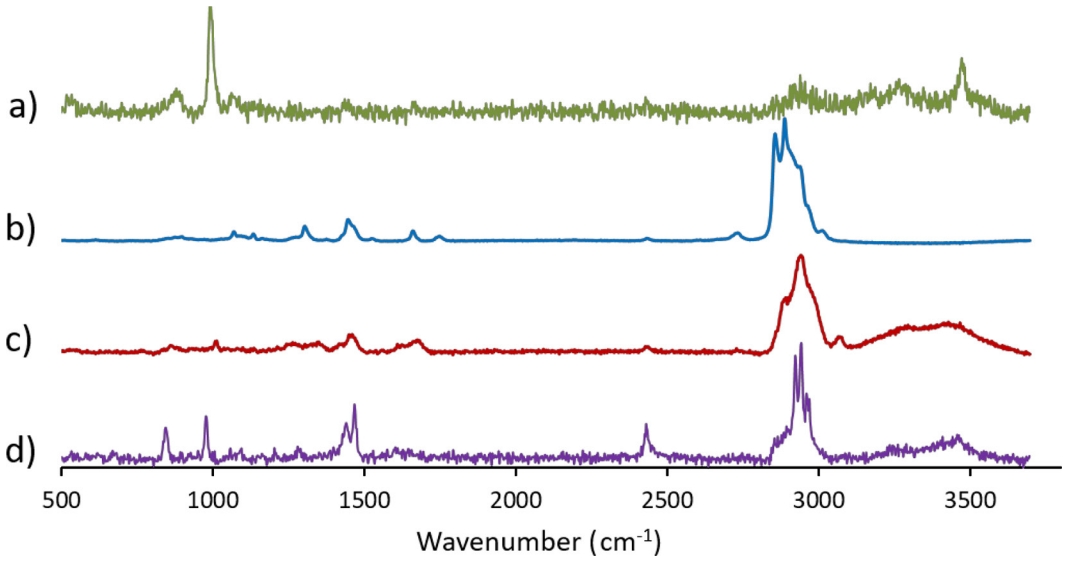

Figure 6. Raman spectra of the 4 main components detected in the spectral data set for the commercial Cheddar cheese sample designated as mid ripening: (a) small microcrystals, (b) fat, (c) protein and water, and (d) bigger microcrystals.

D'Incecco et al. (2016). The absence of peaks in the 2,850 to 3,000 cm^{-1} region also confirms the inorganic origin of this type of crystal. The Raman spectrum of calcium phosphate varies considerably depending on the crystalline form (de Aza et al., 1997) and origin (Sauer et al., 1994; Anjaneyulu et al., 2015), but the presence of the characteristic peaks of PO_4^{3-} in the spectral region corresponding to its internal modes at 995 and 886 cm^{-1} confirmed its presence.

Smith et al. (2017), using a univariate analysis method, were able to correctly identify the distribution of protein in processed cheese. However, this was not the case with the commercial Cheddar cheese samples tested. The proximity of the main band ascribed to phosphate groups to the one corresponding to phenylalanine in proteins (Table 2) explains the overlap of the signal from these 2 components that led to the misidentification. Nevertheless, this was successfully clarified by using a multivariate data processing approach.

Regarding the second type of crystals, which were bigger (see "Microstructural Analysis by Micro-CT"), only one was identified in the micrographs in Figure 7 due to the relatively small areas scanned by confocal Raman microscopy (none were detected by CLSM, with even smaller areas covered). The spectrum of this type of crystal (Figure 6d) exhibited the most intense peaks at 848, 980, 1,443, 1,470, and 2,850 to 3,000 cm^{-1}. This spectrum did not match that of amino acids such as tyrosine or cysteine crystals, previously identified in Cheddar cheese (Tansman et al., 2015). The Raman bands for carboxylic acids and amino groups are generally weak, so despite having these 2 groups in common, the spectra of the various amino acids are quite different (De Gelder et al., 2007). For amino acids containing aromatic rings, such as tyrosine, the most intense band is generally the one corresponding to the trigonal ring breathing of the benzene ring, located around 828 cm^{-1} in the form of a doublet for tyrosine (D'Incecco et al., 2016; Hernández et al., 2016). Although this wavelength is close to one of the main peaks detected in the unknown crystal (Figure 6d), tyrosine does not exhibit intense bands in the region of 1,420 to 1,500 cm^{-1}, generally ascribed to deformations of CH_2 and CH_3 groups in other amino acids (De Gelder et al., 2007). Cysteine, also identified as crystals in Cheddar cheese in previous works (Harper et al., 1953), has an intense Raman peak at 2,565 cm^{-1}, corresponding to the stretching vibration of its SH group, and another one at 682 cm^{-1} (Freire et al., 2017), neither of which were present in the spectrum of the crystals detected in the Cheddar cheese samples in this work.

The other main crystals found in Cheddar cheese are calcium lactate pentahydrate crystals. Lactate salts have been reported to exhibit their main peak around 830 cm^{-1} and also bands corresponding to the asymmetric deformation of CH_3 groups around 1,455 and 1,475 cm^{-1}, as well as peaks ascribed to the stretching vibrations of CH and CH_3 groups in the 2,850 to 3,000 cm^{-1} range (Cassanas et al., 1991; Liato et al., 2016; Ostovar Pour et al., 2019), all consistent with the spectrum shown in Figure 6d. However, calcium lactate pentahydrate has also been described to exhibit a strong, distinct band around 540 cm^{-1}, ascribed to the deformation of OCO groups, that was not present

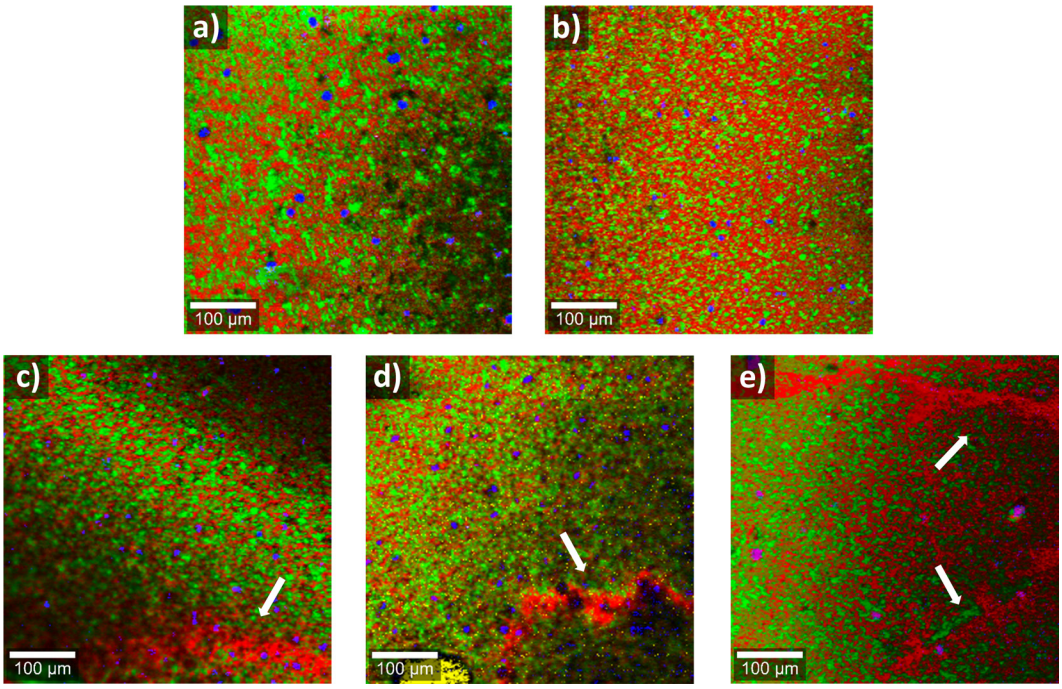

Figure 7. Raman micrographs of the 5 commercial Cheddar cheese samples obtained using a multivariate analysis approach: (a) high fat, (b) low fat, (c) short ripening, (d) mid ripening, and (e) long ripening. Fat distribution is colored in green, protein distribution is shown in red, and blue and yellow colors depict 2 different types of salts. White arrows indicate the presence of curd junctions. The length of the scale bars corresponds to 100 µm.

in the spectra, and they lack the intense peak detected at 980 cm^{-1}, showing only a weak one at around 930 cm^{-1} instead (Cassanas et al., 1991).

To confirm that the spectrum in Figure 6d, identified by applying the basis analysis algorithm to the full data set of the MidRip sample, was accurate and corresponded to the spectrum of the big crystals identified in the section "Microstructural Analysis by Micro-CT," these crystals were identified using the optical camera on the Raman microscope, and individual spectra of the crystals were acquired with a greater signal-to-noise ratio by using a higher integration time (2s) and 10 accumulations. To facilitate a direct comparison of these spectra with those of the different types of salts previously detected in Cheddar cheese, spectra of the commercial salts (i.e., calcium lactate pentahydrate, L-tyrosine, and L-cysteine hydrochloride hydrate) were also acquired. These spectra, together with an optical image of one of the crystals, are shown in Supplemental Figure S5 (https://doi.org/10.17632/4h2gwr26p9.1; Lourenco et al., 2022). Indeed, the spectrum of the crystals was confirmed with the newly acquired spectra, which had a greater signal-to-noise ratio due to the increased integration time and number of accumulations. In these, the band around 540 cm^{-1} characteristic of calcium lactate, although very faint, was detected (Supplemental Figure S5). Tansman et al. (2014) recently demonstrated the presence of 2 different crystalline forms of calcium lactate pentahydrate in Cheddar cheese samples using powder X-ray diffraction, corresponding to 2 enantiomeric forms of the salt (L- and DL-). Johnson (2014) also pointed out that calcium lactate crystals in cheese contain large quantities of entrapped impurities, and these could potentially alter their crystallization. Because the Raman spectra of different crystalline forms of the same organic compound are also different and distinct (Donahue et al., 2011), as previously discussed for calcium phosphate crystals, we hypothesized that the differences between the spectrum of the commercial calcium lactate and the crystal identified in the Cheddar cheese samples might be due to their different crystalline forms. Thus, the bigger crystals were tentatively identified as calcium lactate crystals, and further work combining Raman spectroscopy studies with X-ray diffraction analyses should be performed to confirm this hypothesis.

CONCLUSIONS

This work demonstrated the potential of the micro-CT and confocal Raman microscopy techniques to provide complementary microstructural and compositional information to that obtained through the well-established CLSM technique. Although CLSM provided the most

accurate and spatially resolved distribution of fat and protein, it showed limitations for studying microcrystals in the cheese samples. In contrast, both micro-CT and confocal Raman microscopy allowed identification of two different types of microcrystals, the former being able to provide more meaningful information on their size, shape, and distribution because of the feasibility of scanning larger sample volumes than with the other 2 techniques. Due to the ability of Raman microscopy to provide compositional information, this technique could be used to chemically identify microcrystals in Cheddar cheese, and allowed comparison of the presence of micronutrients such as carotenoids in the samples.

ACKNOWLEDGMENTS

This project was funded by Teagasc, the Irish Agricultural and Food Development Authority. Antonio Lourenco's Research Leaders 2025 postdoctoral funding from the European Union's Horizon 2020 research and innovation program under the Marie Skłodowska-Curie grant agreement number 754380 is gratefully acknowledged. This research was supported using resources of the VetCore Facility (VetImaging) of the University of Veterinary Medicine Vienna and the National Food Imaging Centre (NFIC) at Teagasc. The authors have not stated any conflicts of interest.

REFERENCES

Anjaneyulu, U., D. Pattanayak, and D. Vijayalakshmi. 2015. Snail shell derived natural hydroxyapatite: Effects on NIH-3T3 cells for orthopedic applications. Mater. Manuf. Process. 31:206–216.

Anvari, M., and H. S. Joyner. 2018. Concentrated emulsions as novel fat replacers in reduced-fat and low-fat Cheddar cheeses. Part 1. Rheological and microstructural characterization. Int. Dairy J. 86:76–85. https://doi.org/10.1016/j.idairyj.2018.06.017.

Auty, M. A., M. Twomey, T. P. Guinee, and D. M. Mulvihill. 2001. Development and application of confocal scanning laser microscopy methods for studying the distribution of fat and protein in selected dairy products. J. Dairy Res. 68:417–427. https://doi.org/10.1017/S0022029901004873.

Ayala-Bribiesca, E., M. Lussier, D. Chabot, S. L. Turgeon, and M. Britten. 2016. Effect of calcium enrichment of Cheddar cheese on its structure, in vitro digestion and lipid bioaccessibility. Int. Dairy J. 53:1–9. https://doi.org/10.1016/j.idairyj.2015.09.002.

Baker, D. R., L. Mancini, M. Polacci, M. D. Higgins, G. A. R. Gualda, R. J. Hill, and M. L. Rivers. 2012. An introduction to the application of X-ray microtomography to the three-dimensional study of igneous rocks. Lithos 148:262–276. https://doi.org/10.1016/j.lithos.2012.06.008.

Benito-González, I., M. Martínez-Sanz, A. López-Rubio, and L. G. Gómez-Mascaraque. 2020. Confocal Raman imaging as a useful tool to understand the internal microstructure of multicomponent aerogels. J. Raman Spectrosc. 51:2022–2035. https://doi.org/10.1002/jrs.5936.

Berg, S., D. Kutra, T. Kroeger, C. N. Straehle, B. X. Kausler, C. Haubold, M. Schiegg, J. Ales, T. Beier, M. Rudy, K. Eren, J. I. Cervantes, B. Xu, F. Beuttenmueller, A. Wolny, C. Zhang, U. Koethe, F. A. Hamprecht, and A. Kreshuk. 2019. Ilastik: Interactive machine learning for (bio) image analysis. Nat. Methods 16:1226–1232. https://doi.org/10.1038/s41592-019-0582-9.

Bernardini, F., C. Tuniz, and F. Zanini. 2019. Chapter 2 - X-ray computed microtomography for paleoanthropology, archaeology, and cultural heritage. Pages 25–45 in Nanotechnologies and Nanomaterials for Diagnostic, Conservation and Restoration of Cultural Heritage. G. Lazzara and R. Fakhrullin, ed. Elsevier.

Bowland, E. L., and E. A. Foegeding. 2001. Small strain oscillatory shear and microstructural analyses of a model processed cheese. J. Dairy Sci. 84:2372–2380. https://doi.org/10.3168/jds.S0022-0302(01)74686-3.

Butler, H. J., L. Ashton, B. Bird, G. Cinque, K. Curtis, J. Dorney, K. Esmonde-White, N. J. Fullwood, B. Gardner, P. L. Martin-Hirsch, M. J. Walsh, M. R. McAinsh, N. Stone, and F. L. Martin. 2016. Using Raman spectroscopy to characterize biological materials. Nat. Protoc. 11:664–687. https://doi.org/10.1038/nprot.2016.036.

Cafarelli, B., A. Spada, J. Laverse, V. Lampignano, and M. A. Del Nobile. 2014. An insight into the bread bubble structure: An X-ray microtomography approach. Food Res. Int. 66:180–185. https://doi.org/10.1016/j.foodres.2014.08.036.

Cassanas, G., M. Morssli, E. Fabregue, and L. Bardet. 1991. Vibrational spectra of lactic acid and lactates. J. Raman Spectrosc. 22:409–413. https://doi.org/10.1002/jrs.1250220709.

Chaichi, A., A. Prasad, and M. R. Gartia. 2018. Raman spectroscopy and microscopy applications in cardiovascular diseases: From molecules to organs. Biosensors (Basel) 8:107. https://doi.org/10.3390/bios8040107.

Chandan, R. C. 2014. CHEESE | Cheese in the marketplace. Pages 384–394 in Encyclopedia of Food Microbiology. 2nd ed. C. A. Batt and M. L. Tortorello, ed. Academic Press.

Conte, A., J. Laverse, C. Costa, V. Lampignano, M. A. Previtali, and M. A. Del Nobile. 2017. Conventional or blast freezing prior to frozen storage to preserve properties of fiordilatte cheese. J. Food Process. Preserv. 41:e13235. https://doi.org/10.1111/jfpp.13235.

Czamara, K., K. Majzner, M. Z. Pacia, K. Kochan, A. Kaczor, and M. Baranska. 2015. Raman spectroscopy of lipids: A review. J. Raman Spectrosc. 46:4–20. https://doi.org/10.1002/jrs.4607.

D'Incecco, P., S. Limbo, F. Faoro, J. Hogenboom, V. Rosi, S. Morandi, and L. Pellegrino. 2016. New insight on crystal and spot development in hard and extra-hard cheeses: Association of spots with incomplete aggregation of curd granules. J. Dairy Sci. 99:6144–6156. https://doi.org/10.3168/jds.2016-11050.

de Aza, P. N., F. Guitián, C. Santos, S. de Aza, R. Cuscó, and L. Artús. 1997. Vibrational properties of calcium phosphate compounds. 2. Comparison between hydroxyapatite and β-tricalcium phosphate. Chem. Mater. 9:916–922. https://doi.org/10.1021/cm9604266.

De Gelder, J., K. De Gussem, P. Vandenabeele, and L. Moens. 2007. Reference database of Raman spectra of biological molecules. J. Raman Spectrosc. 38:1133–1147.

Donahue, M., E. Botonjic-Sehic, D. Wells, and C. Brown. 2011. Understanding infrared and Raman spectra of pharmaceutical polymorphs. Am. Pharm. Rev. 14(2):.

Fenelon, M., and T. Guinee. 1999. The effect of milk fat on Cheddar cheese yield and its prediction, using modifications of the Van Slyke cheese yield formula. J. Dairy Sci. 82:2287–2299. https://doi.org/10.3168/jds.S0022-0302(99)75477-9.

Freire, P. T. C., F. M. Barboza, J. A. Lima, F. E. A. Melo, and J. Mendes Filho. 2017. Chapter 10: Raman spectroscopy of amino acid crystals. In Raman Spectroscopy and Applications. K. Maaz, ed. IntechOpen.

Frisullo, P., F. Licciardello, G. Muratore, and M. A. Del Nobile. 2010. Microstructural Characterization of Multiphase Chocolate Using X-Ray Microtomography. J. Food Sci. 75:E469–E476. https://doi.org/10.1111/j.1750-3841.2010.01745.x.

Gallier, S., K. C. Gordon, R. Jiménez-Flores, and D. W. Everett. 2011. Composition of bovine milk fat globules by confocal Raman microscopy. Int. Dairy J. 21:402–412. https://doi.org/10.1016/j.idairyj.2011.01.008.

Gómez-Mascaraque, L. G., K. Kilcawley, D. Hennessy, J. T. Tobin, and T. F. O'Callaghan. 2020. Raman spectroscopy: A rapid method to assess the effects of pasture feeding on the nutritional quality of butter. J. Dairy Sci. 103:8721–8731. https://doi.org/10.3168/jds.2020-18716.

Gómez-Mascaraque, L. G., and S. C. Pinho. 2021. Microstructural analysis of whey/soy protein isolate mixed gels using confocal Raman microscopy. Foods 10:2179. https://doi.org/10.3390/foods10092179.

Gómez-Mascaraque, L. G., C. Tran, T. O'Callaghan, and S. A. Hogan. 2021. Use of confocal Raman imaging to understand the microstructure of anhydrous milk fat-based oleogels. Food Structure 30:100228.

Guggisberg, D., P. Schuetz, H. Winkler, R. Amrein, E. Jakob, M.-T. Fröhlich-Wyder, S. Irmler, W. Bisig, I. Jerjen, M. Plamondon, J. Hofmann, A. Flisch, and D. Wechsler. 2015. Mechanism and control of the eye formation in cheese. Int. Dairy J. 47:118–127. https://doi.org/10.1016/j.idairyj.2015.03.001.

Guinee, T. P., E. Mulholland, J. Kelly, and D. Callaghan. 2007. Effect of protein-to-fat ratio of milk on the composition, manufacturing efficiency, and yield of Cheddar cheese. J. Dairy Sci. 90:110–123. https://doi.org/10.3168/jds.S0022-0302(07)72613-9.

Guinee, T. P., M. A. Auty, and M. A. Fenelon. 2000. The effect of fat content on the rheology, microstructure and heat-induced functional characteristics of Cheddar cheese. Int. Dairy J. 10:277–288. https://doi.org/10.1016/S0958-6946(00)00048-0.

Gunasekaran, S., and K. Ding. 1999. Three-dimensional characteristics of fat globules in Cheddar cheese. J. Dairy Sci. 82:1890–1896. https://doi.org/10.3168/jds.S0022-0302(99)75423-8.

Haedelt, J., S. T. Beckett, and K. Niranjan. 2007. Bubble-included chocolate: Relating structure with sensory response. J. Food Sci. 72:E138–E142. https://doi.org/10.1111/j.1750-3841.2007.00313.x.

Harper, W., A. Swanson, and H. Sommer. 1953. Observations on the chemical composition of white particles in several lots of Cheddar cheese. J. Dairy Sci. 36:368–372. https://doi.org/10.3168/jds.S0022-0302(53)91505-7.

Hernández, B., Y. M. Coïc, F. Pflüger, S. G. Kruglik, and M. Ghomi. 2016. All characteristic Raman markers of tyrosine and tyrosinate originate from phenol ring fundamental vibrations. J. Raman Spectrosc. 47:210–220. https://doi.org/10.1002/jrs.4776.

Huc, D., S. Challois, M. Monziols, C. Michon, and F. Mariette. 2014. Spatial characterisation of eye-growing kinetics in semi-hard cheeses with propionic acid fermentation. Int. Dairy J. 39:259–269. https://doi.org/10.1016/j.idairyj.2014.06.010.

Huen, J., C. Weikusat, M. Bayer-Giraldi, I. Weikusat, L. Ringer, and K. Lösche. 2014. Confocal Raman microscopy of frozen bread dough. J. Cereal Sci. 60:555–560. https://doi.org/10.1016/j.jcs.2014.07.012.

IMARC. 2022. Cheese Market: Global Industry Trends, Share, Size, Growth, Opportunity and Forecast 2022–2027. IMARC Services Private Limited.

Jensen, B. B., Z. J. Glover, S. M. M. Pedersen, U. Andersen, L. Duelund, and J. R. Brewer. 2019. Label free noninvasive spatially resolved NaCl concentration measurements using Coherent Anti-Stokes Raman Scattering microscopy applied to butter. Food Chem. 297:124881. https://doi.org/10.1016/j.foodchem.2019.05.155.

Johnson, M. 2014. Crystallization in cheese. Dairy pipeline. Wisconsin Center for Dairy Research 26:1–5.

Kalab, M., R. J. Lowrie, and D. Nichols. 1982. Detection of curd granule and milled curd junctions in Cheddar cheese. J. Dairy Sci. 65:1117–1121. https://doi.org/10.3168/jds.S0022-0302(82)82320-5.

Khanal, B. K. S., B. Bhandari, S. Prakash, D. Liu, P. Zhou, and N. Bansal. 2018. Modifying textural and microstructural properties of low fat Cheddar cheese using sodium alginate. Food Hydrocoll. 83:97–108. https://doi.org/10.1016/j.foodhyd.2018.03.015.

Lagaude, A., L. Fernandez, J.-L. Cuq, and S. Marchesseau. 2004. Characterization of curd formation during the rennet coagulation of milk by an optical microscopic method. Int. Dairy J. 14:1033–1039. https://doi.org/10.1016/j.idairyj.2004.05.001.

Lamichhane, P., P. Sharma, D. Kennedy, A. L. Kelly, and J. J. Sheehan. 2019. Microstructure and fracture properties of semi-hard cheese: Differentiating the effects of primary proteolysis and calcium solubilization. Food Res. Int. 125:108525. https://doi.org/10.1016/j.foodres.2019.108525.

Lei, T., and D.-W. Sun. 2019. Developments of nondestructive techniques for evaluating quality attributes of cheeses: A review. Trends Food Sci. Technol. 88:527–542. https://doi.org/10.1016/j.tifs.2019.04.013.

Liato, V., S. Labrie, and M. Aïder. 2016. Electro-activation of potassium acetate, potassium citrate and calcium lactate: Impact on solution acidity, redox potential, vibrational properties of Raman spectra and antibacterial activity on *E. coli* O157: H7 at ambient temperature. Springerplus 5:1760. https://doi.org/10.1186/s40064-016-3453-1.

Licciardello, F., P. Frisullo, J. Laverse, G. Muratore, and M. A. Del Nobile. 2012. Effect of sugar, citric acid and egg white type on the microstructural and mechanical properties of meringues. J. Food Eng. 108:453–462. https://doi.org/10.1016/j.jfoodeng.2011.08.021.

Lim, K., and M. Barigou. 2004. X-ray micro-computed tomography of cellular food products. Food Res. Int. 37:1001–1012. https://doi.org/10.1016/j.foodres.2004.06.010.

Limaye, A. 2012. Drishti: A Volume Exploration and Presentation Tool. Vol. 8506. SPIE Optical Engineering + Applications. SPIE.

Lourenco, A., S. Handschuh, M. Fenelon, and L. G. Gomez-Mascaraque. 2022. Supplementary Material for "X-ray computerised microtomography and confocal Raman microscopy as complementary techniques for the microstructural characterisation of Cheddar cheese." Mendeley Data, V1. https://doi.org/10.17632/4h2gwr26p9.1.

Lv, J., W. Zhang, S. Liu, R. Chen, J. Feng, S. Zhou, and Y. Liu. 2016. Analysis of 52 automotive coating samples for forensic purposes with Fourier transform infrared spectroscopy (FTIR) and Raman microscopy. Environ. Forensics 17:59–67. https://doi.org/10.1080/15275922.2015.1091403.

Marcott, C., M. Padalkar, and N. Pleshko. 2017. 3.23 Infrared and Raman microscopy and imaging of biomaterials at the micro and nano scale. Pages 498–518 in Comprehensive Biomaterials II. P. Ducheyne, ed. Elsevier, Oxford.

McSweeney, P. L. H., G. Ottogalli, and P. F. Fox. 2017. Chapter 31 - Diversity and classification of cheese varieties: An overview. Pages 781–808 in Cheese. 4th ed. P. L. H. McSweeney, P. F. Fox, P. D. Cotter, and D. W. Everett, ed. Academic Press.

Nickless, E., and S. Holroyd. 2020. Raman imaging of protein in a model cheese system. J. Spectral Imaging 9:a9. https://doi.org/10.1255/jsi.2020.a9.

O'Reilly, C. E., A. L. Kelly, J. C. Oliveira, P. M. Murphy, M. A. E. Auty, and T. P. Beresford. 2003. Effect of varying high-pressure treatment conditions on acceleration of ripening of cheddar cheese. Innov. Food Sci. Emerg. Technol. 4:277–284. https://doi.org/10.1016/S1466-8564(03)00037-7.

O'Sullivan, D. J., P. L. H. McSweeney, P. D. Cotter, L. Giblin, and J. J. Sheehan. 2016. Compromised *Lactobacillus helveticus* starter activity in the presence of facultative heterofermentative *Lactobacillus casei* DPC6987 results in atypical eye formation in Swiss-type cheese. J. Dairy Sci. 99:2625–2640. https://doi.org/10.3168/jds.2015-10503.

Ong, L., R. R. Dagastine, M. A. E. Auty, S. E. Kentish, and S. L. Gras. 2011a. Coagulation temperature affects the microstructure and composition of full fat Cheddar cheese. Dairy Sci. Technol. 91:739–758. https://doi.org/10.1007/s13594-011-0033-6.

Ong, L., R. R. Dagastine, S. E. Kentish, and S. L. Gras. 2011b. Microstructure of milk gel and cheese curd observed using cryo scanning electron microscopy and confocal microscopy. Lebensm. Wiss. Technol. 44:1291–1302. https://doi.org/10.1016/j.lwt.2010.12.026.

Ong, L., R. R. Dagastine, S. E. Kentish, and S. L. Gras. 2012. The effect of pH at renneting on the microstructure, composition and texture of Cheddar cheese. Food Res. Int. 48:119–130. https://doi.org/10.1016/j.foodres.2012.02.020.

Ong, L., R. R. Dagastine, S. E. Kentish, and S. L. Gras. 2013. The effect of calcium chloride addition on the microstructure and composition of Cheddar cheese. Int. Dairy J. 33:135–141. https://doi.org/10.1016/j.idairyj.2013.03.002.

Ong, L., R. C. Lawrence, J. Gilles, L. K. Creamer, V. L. Crow, H. A. Heap, C. G. Honoré, K. A. Johnston, P. K. Samal, I. B. Powell, and S. L. Gras. 2017. Chapter 33 - Cheddar cheese and related

dry-salted cheese varieties. Pages 829–863 in Cheese. 4th ed. P. L. H. McSweeney, P. F. Fox, P. D. Cotter, and D. W. Everett, ed. Academic Press.

Ong, L., K. Soodam, S. E. Kentish, I. B. Powell, and S. L. Gras. 2015. The addition of calcium chloride in combination with a lower draining pH to change the microstructure and improve fat retention in Cheddar cheese. Int. Dairy J. 46:53–62. https://doi.org/10.1016/j.idairyj.2014.07.003.

Ostovar Pour, S., S. M. Fowler, D. L. Hopkins, P. J. Torley, H. Gill, and E. W. Blanch. 2019. Investigation of chemical composition of meat using spatially off-set Raman spectroscopy. Analyst 144:2618–2627. https://doi.org/10.1039/C8AN01958D.

Pikhur, O. L., Y. V. Plotkina, and A. M. Kulkov. 2020. Using x-ray computed microtomography for investigation of the morphology and composition of the hard tooth tissue. Pages 221–232 in Processes and Phenomena on the Boundary Between Biogenic and Abiogenic Nature. Springer.

Piovesan, A., V. Vancauwenberghe, W. Aregawi, M. A. Delele, E. Bongaers, M. de Schipper, K. van Bommel, M. Noort, P. Verboven, and B. Nicolai. 2020. Designing mechanical properties of 3D printed cookies through computer aided engineering. Foods 9:1804. https://doi.org/10.3390/foods9121804.

Pu, H., L. Lin, and D. W. Sun. 2019. Principles of hyperspectral microscope imaging techniques and their applications in food quality and safety detection: A review. Compr. Rev. Food Sci. Food Saf. 18:853–866. https://doi.org/10.1111/1541-4337.12432.

Ray, C. A., A. Gholamhosseinpour, R. Ipsen, and A. B. Hougaard. 2016. The effect of age on Cheddar cheese melting, rheology and structure, and on the stability of feed for cheese powder manufacture. Int. Dairy J. 55:38–43. https://doi.org/10.1016/j.idairyj.2015.11.009.

Roeffaers, M. B. J., X. Zhang, C. W. Freudiger, B. G. Saar, X. S. Xie, M. van Ruijven, G. van Dalen, and C. Xiao. 2011. Label-free imaging of biomolecules in food products using stimulated Raman microscopy. J. Biomed. Opt. 16:021118. https://doi.org/10.1117/1.3516591.

Rogers, N. R., D. J. McMahon, C. R. Daubert, T. K. Berry, and E. A. Foegeding. 2010. Rheological properties and microstructure of Cheddar cheese made with different fat contents. J. Dairy Sci. 93:4565–4576. https://doi.org/10.3168/jds.2010-3494.

Sauer, G. R., W. B. Zunic, J. R. Durig, and R. E. Wuthier. 1994. Fourier transform Raman spectroscopy of synthetic and biological calcium phosphates. Calcif. Tissue Int. 54:414–420. https://doi.org/10.1007/BF00305529.

Schindelin, J., I. Arganda-Carreras, E. Frise, V. Kaynig, M. Longair, T. Pietzsch, S. Preibisch, C. Rueden, S. Saalfeld, B. Schmid, J.-Y. Tinevez, D. J. White, V. Hartenstein, K. Eliceiri, P. Tomancak, and A. Cardona. 2012. Fiji: An open-source platform for biological-image analysis. Nat. Methods 9:676–682. https://doi.org/10.1038/nmeth.2019.

Singh, S. S., T. J. Stannard, X. Xiao, and N. Chawla. 2017. In situ x-ray microtomography of stress corrosion cracking and corrosion fatigue in aluminum alloys. J. Miner. Met. Mater. Soc. 69:1404–1414. https://doi.org/10.1007/s11837-017-2413-8.

Smith, G. P., S. E. Holroyd, D. C. Reid, and K. C. Gordon. 2017. Raman imaging processed cheese and its components. J. Raman Spectrosc. 48:374–383. https://doi.org/10.1002/jrs.5054.

Sommer, C., C. Straehle, U. Koethe, and F. A. Hamprecht. 2011. Ilastik: Interactive learning and segmentation toolkit. Pages 230–233 in Proc. 2011 IEEE International Symposium on Biomedical Imaging: From Nano to Macro. IEEE.

Soodam, K., L. Ong, I. B. Powell, S. E. Kentish, and S. L. Gras. 2014. The effect of milk protein concentration on the microstructure and textural properties of full fat cheddar cheese during ripening. Food Bioprocess Technol. 7:2912–2922. https://doi.org/10.1007/s11947-014-1342-6.

Soodam, K., L. Ong, I. B. Powell, S. E. Kentish, and S. L. Gras. 2015a. Effect of calcium chloride addition and draining pH on the microstructure and texture of full fat Cheddar cheese during ripening. Food Chem. 181:111–118. https://doi.org/10.1016/j.foodchem.2015.01.135.

Soodam, K., L. Ong, I. B. Powell, S. E. Kentish, and S. L. Gras. 2015b. Effect of rennet on the composition, proteolysis and microstructure of reduced-fat Cheddar cheese during ripening. Dairy Sci. Technol. 95:665–686. https://doi.org/10.1007/s13594-015-0250-5.

Soodam, K., L. Ong, I. B. Powell, S. E. Kentish, and S. L. Gras. 2017. Effect of elevated temperature on the microstructure of full fat Cheddar cheese during ripening. Food Structure 14:8–16. https://doi.org/10.1016/j.foostr.2017.05.003.

Stephani, R., K. S. Oliveira, C. E. R. de Almeida, Í. T. Perrone, A. F. de Carvalho, L. F. C. de Oliveira, and M. R. Almeida. 2017. Raman spectroscopy as a tool to identify modification of whey protein concentrate (WPC) during shelf life. Food Packag. Shelf Life 11:1–9. https://doi.org/10.1016/j.fpsl.2016.10.001.

Tansman, G. F., P. S. Kindstedt, and J. M. Hughes. 2015. Crystal fingerprinting: elucidating the crystals of Cheddar, Parmigiano-Reggiano, Gouda, and soft washed-rind cheeses using powder x-ray diffractometry. Dairy Sci. Technol. 95:651–664. https://doi.org/10.1007/s13594-015-0225-6.

Tansman, G. F., P. S. Kindstedt, and J. M. Hughes. 2014. Powder X-ray diffraction can differentiate between enantiomeric variants of calcium lactate pentahydrate crystal in cheese. J. Dairy Sci. 97:7354–7362. https://doi.org/10.3168/jds.2014-8277.

Tejeda, H. A., and M.-K. Kim. 2021. Dynamic price relationships and price discovery among cheese markets. Int. Food Agribus. Manag. Rev. 24:1–13. https://doi.org/10.22434/IFAMR2019.0206.

van den Boogert, T., M. van Hoof, S. Handschuh, R. Glueckert, N. Guinand, J.-P. Guyot, H. Kingma, A. Perez-Fornos, B. Seppen, L. Johnson Chacko, A. Schrott-Fischer, and R. van de Berg. 2018. Optimization of 3D-visualization of micro-anatomical structures of the human inner ear in osmium tetroxide contrast enhanced micro-CT scans. Front. Neuroanat. 12:41. https://doi.org/10.3389/fnana.2018.00041.

Willner, M., M. Viermetz, M. Marschner, K. Scherer, C. Braun, A. Fingerle, P. Noël, E. Rummeny, F. Pfeiffer, and J. Herzen. 2016. Quantitative three-dimensional imaging of lipid, protein, and water contents via x-ray phase-contrast tomography. PLOS One 11:e0151889. https://doi.org/10.1371/journal.pone.0151889.

Yasseri, M., D. Schüpfer, M. Weinhold, L. Chen, H. Kamila, E. Müller, J. de Boor, and P. J. Klar. 2020. Comparing Raman mapping and electron microscopy for characterizing compositional gradients in thermoelectric materials. Scr. Mater. 179:61–64. https://doi.org/10.1016/j.scriptamat.2020.01.002.

Zapata, F., and C. García-Ruiz. 2017. Analysis of different materials subjected to open-air explosions in search of explosive traces by Raman microscopy. Forensic Sci. Int. 275:57–64. https://doi.org/10.1016/j.forsciint.2017.02.032.

Zhang, C., D. Zhang, and J.-X. Cheng. 2015. Coherent Raman scattering microscopy in biology and medicine. Annu. Rev. Biomed. Eng. 17:415–445. https://doi.org/10.1146/annurev-bioeng-071114-040554.